Comprehensive Imaging of C-2W Plasmas: Instruments and Applications[a)]

E. M. Granstedt,[1, b)] D. Gupta,[1] J. Sweeney,[1] M. Tobin,[1] M. Dikovsky,[2] and the TAE Team[1]
[1)] *TAE Technologies, Inc., 19631 Pauling, Foothill Ranch, CA 92610*
[2)] *Google Inc., 1600 Amphitheatre Parkway, Mountain View, CA 94043*

(Dated: 30 November 2020)

The C-2W device ("Norman"),[1] has produced and sustained beam-driven field-reversed configuration (FRC) plasmas embedded in a magnetic mirror geometry using neutral beams and end-bias electrodes located in expander divertors. Many discrete vessels comprise this device, and a suite of spatially and radiometrically calibrated, high-speed camera systems have been deployed to visualize the plasma throughout.

Besides global visualization of the plasma evolution, this imaging suite has been used in a variety of applications. Reconstruction of the magnetic field in the equilibrium vessel is complicated by eddy currents in conducting structures and thus far, non-perturbative measurements of internal field have not been available. Tomographic reconstruction of O^{4+} impurity emission provides an independent check of magnetic modeling and indirect evidence for field reversal within the FRC.

Voltages up to 3.5 kV are applied to electrodes in the expander divertors to control the radial electric field in the plasma located on open field-lines. This has been shown to improve the macroscopic stability of the FRC; however, a full model for how electrode potentials propagate to the center of the plasma is the subject of ongoing work. Imaging in the expander divertors is used to study gas ionization and to identify metal arcing from electrode surfaces.

I. INTRODUCTION

The C-2W device ("Norman"),[1] which produced its first plasma in 2017, was built to further the progress towards a steady-state, beam-driven field-reversed configuration (FRC) fusion reactor. Dynamic formation and merging has been used to generate an initial FRC, then neutral beams and power from end-bias electrodes have sustained the FRC embedded in a magnetic mirror plasma for ∼30 ms, limited by power supply energy storage. As in many magnetic fusion devices,[2–4] high-speed cameras equipped with narrow-band interference filters were used on the predecessor device to visualize the global discharge evolution, macroscopic instabilities, plasma-material interaction, particle fueling, and other phenomena. Nearly all C-2W systems were entirely new compared to those on the previous C-2U[6,7] machine; some presented new needs and challenges for filtered high-speed imaging.

For example, additional expander divertors with cryo-cooled surfaces were placed between the confinement vessel and formation section to provide additional gas pumping and so that biased electrodes could be placed closer to the FRC. End-bias electrodes were improved to allow operation at >3.5 kV, driven by a programmable power supply capable of delivering up to 7 kA. High voltage surfaces in four vacuum vessels made it necessary to develop a common divertor imaging platform which could identify off-normal events (e.g., bipolar arcing) and estimate the gas ionization rate.

High-speed visualization of the FRC plasma in the CV became more critical, because although end-biasing was used to stabilize a deleterious $n = 2$ deformation mode,[8,9] if operated incorrectly it could also drive other modes. To provide opportunity to develop magnetic control, the confinement vessel was constructed from 1/4" Inconel to reduce the resistive wall time. This reduced the effect of wall stabilization compared to C-2U. It also made determination of the excluded flux profile more difficult because of the shorter decay time for vessel eddy currents and the longer plasma duration. Passive impurity imaging from multiple views supplied data for tomographic reconstruction to serve as a sanity-check for the excluded-flux radius inferred from wall-mounted magnetic sensors and indirect evidence for field reversal.

Finally, to maximize light throughput and reduce cost, imaging instruments were attached directly to the vacuum vessel in regions with magnetic field up to xx kG. Reliable operation in this environment was achieved with specific commercial cameras and careful component placement.

This paper is organized as follows: Section I of this paper describes the suite of imaging instruments on C-2W. Section II describes instability visualization and tomographic reconstruction, two applications for imaging the FRC plasma in the confinement vessel. Section III describes the estimate of ionization rate from divertor camera imaging data and off-normal event identification, two needs for imaging in the divertor vessels.

[a)] Contributed paper published as part of the Proceedings of the 23rd Topical Conference on High-Temperature Plasma Diagnostics, Santa Fe, New Mexico, December, 2020.
[b)] Electronic mail: egranstedt@tae.com

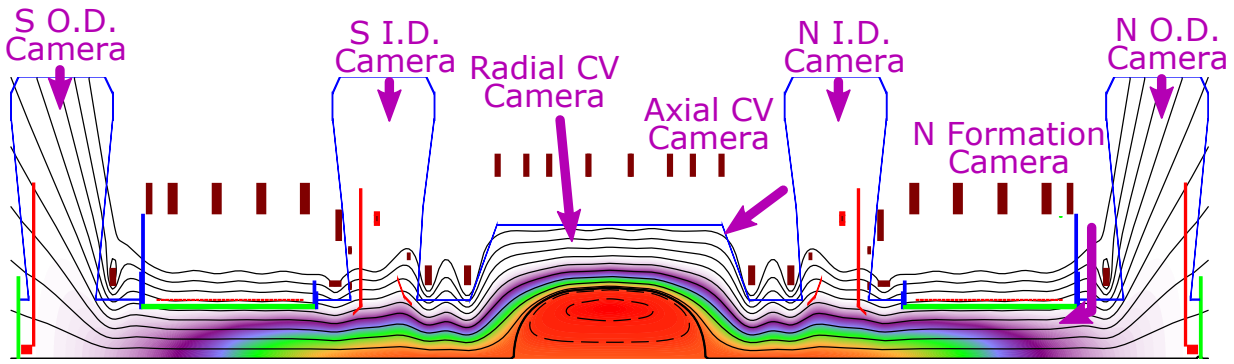

FIG. 1. C-2W device showing location and orientation of imaging instruments described in this paper.

view	camera	viewport	imaging lens	H ×V px @ frame rate
CV radial	Phantom Miro Lab310	re-entrant sapphire	Theia ML410M	384×384 @ 19.5 kfps
CV axial	Phantom Miro Lab310	quartz	Fujinon CF25HA-1	384×384 @ 19.5 kfps
N. inner div.	Edgertronic SC1	quartz	Fujinon CF16HA-1	400×480 @ 2.36 kfps
S. inner div.	Edgertronic SC1	quartz	Fujinon CF12.5HA-1	256×256 @ 6.15 kfps
N. formation	Edgertronic SC2+	re-entrant sapphire	Fujinon CF25HA-1	512×288 @ 10.9 kfps
N. outer div.	Edgertronic SC2+	quartz	Fujinon CF12.5HA-1	512×288 @ 10.9 kfps
S. outer div.	Phantom v5.1	quartz	Fujinon CF16HA-1	384×384 @ 9.1 kfps

TABLE I. Basic specifications for each imaging instrument along with the typical frame size and frame rate.

II. IMAGING INSTRUMENT SUITE

A. Design and layout

One of the challenges with obtaining a comprehensive view of the C-2W plasma is the total length (24 m) and number of vessels which comprise the C-2W device. As a result, the imaging suite is composed of seven instruments. Their locations and viewing geometry are illustrated in Fig. 1, while their specifications are listed in table I. The highest speed cameras were installed on the confinement vessel in order to observe the FRC with the highest time resolution. One camera with a re-entrant viewport observes the confinement vessel plasma with a fisheye lens to get a wide-angle radial view, while a second observes the plasma from the end-bell region and provides an axial view. These nearly orthogonal views enable tomographic reconstruction and tracking of deuterium pellets and compact tori which are being developed as alternative fueling techniques.

A camera with re-entrant viewport and mirror are installed between the formation section and mirror plug coil to view the theta-pinch formation process and monitor the stability of this long cylindrical plasma column. The primary gas injection location is at this same axial position, so the Balmer-α emission in this region serves as a proxy for the ionization rate into the mirror plasma surrounding the FRC. These three camera instruments have 10-position Ethernet-controlled filter wheels and are similar to those used on C-2U,[10] however use a phenolic plate to electrically isolate the instrument from the vacuum vessel.

Each of the four divertors is equipped with an imaging instrument built on a common platform consisting of a mechanical support, phenolic mounting plate to isolate the instrument electrically from the vacuum vessel, and a four position Ethernet-controlled filter wheel (holding 2 in dia. narrow-band interference filters) with position feedback.

In all cases, imaging lenses which view the plasma are coupled to the camera by periscopes consisting of discrete achromatic lenses from optics manufacturers and/or commercial multi-element photography lenses.

More detail of the electronics, communication, and control of the instruments can be found in Ref..[10] The instruments are radiometrically calibrated *ex-situ* and spatially calibrated *in-situ* following the procedure in Ref..[11]

B. Performance in magnetic environment

During the initial build-out of C-2W, a Phantom v5.1 camera was used for the formation view. This camera would power-cycle when the magnetic field generated by the nearby DC (not pulsed-power) magnets exceeded 340 G, calculated by a finite-element analysis code. By swapping the camera with a Sanstreak Edgertronic SC2+ and powering the camera from an AC-DC power supply (rather than after a DC-DC converter), the instrument has been able to operate reliably in a magnetic field up to 1.7 kG.

The Phantom Miro Lab310 camera which observes the confinement vessel plasma from an end-on view also operates in a relatively high magnetic field, up to $\sim$ kG. During initial testing, the camera would occasionally appear to operate normally, but recorded data would look like readout noise with no illumination. During a shot with magnetic field ramping-up, the calibration black reference flag was seen to move in front of the sensor. By removing this flag assembly, the instrument has operated reliably at fields up to about y kG.

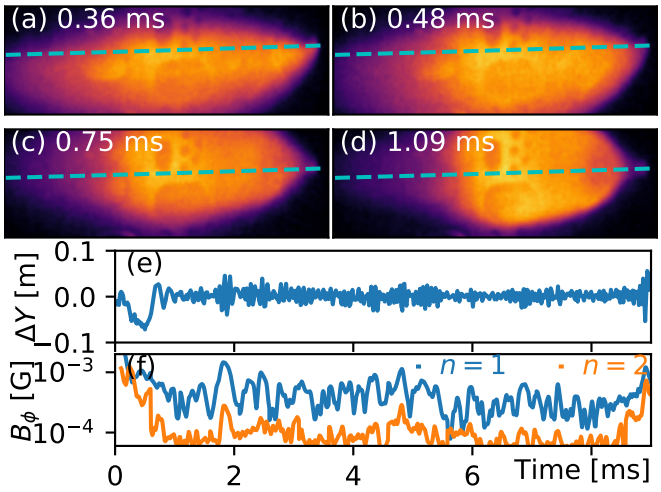

FIG. 2. (a)–(d) Images from the radial CV camera with the machine axis indicated by a dashed line. (e) Vertical position of emission centroid. (f) Amplitude of azimuthal modes determined from HOSVD analysis of Mirnov probe signals.

III. GLOBAL VISUALIZATION OF CV PLASMA

Spectral line emission resulting from electron-impact excitation of instrinsic impurities is observed by the imaging cameras to visualize the plasma. Oxygen is generally the dominant impurity on C-2W, and the 650 nm spectral line from the O^{4+} 3d→3p transition is frequently monitored by the cameras in the confinement vessel due to the high optics transmission and good sensor quantum efficiency at this wavelength.

Processed movies available within a few minutes of each shot provide insight into the evolution, dynamics, and macroscopic stability of each shot. Fig. 2 is an interesting example of a shot that began displaced from the axis (Fig. 2a), but was re-centered within about 1 ms (Fig. 2b-d), presumably by the combined effect of the neutral beams and end-biasing. The vertical displacement of the emission centroid (Fig. 2e) can be used in conjunction with signals from Mirnov probes to model the dynamics.

For more quantitative insight into the plasma evolution, the emissivity can be tomographically reconstructed. The current emissivity reconstruction assumes axisymmetry, and each value on the vessel-filling (r, z) grid represents a ring in 3D space. As a first step to computing the projection matrix from the reconstruction grid to camera pixels, each ring is remapped into a 3D Cartesian grid using a high-order polygon approximation. Next, several sightlines for each pixel and camera are broken into a large number of uniform-length segments; the projection from the 3D grid to the camera sensor is found from the length of each segment through each 3D grid cell. The composition of these two projection operations gives the projection from the (r, z) grid to the camera pixels. Splitting the projection matrix computation into these two steps would provide a way to allow displacements in the axis of symmetry without having to re-calculate the full projection matrix.

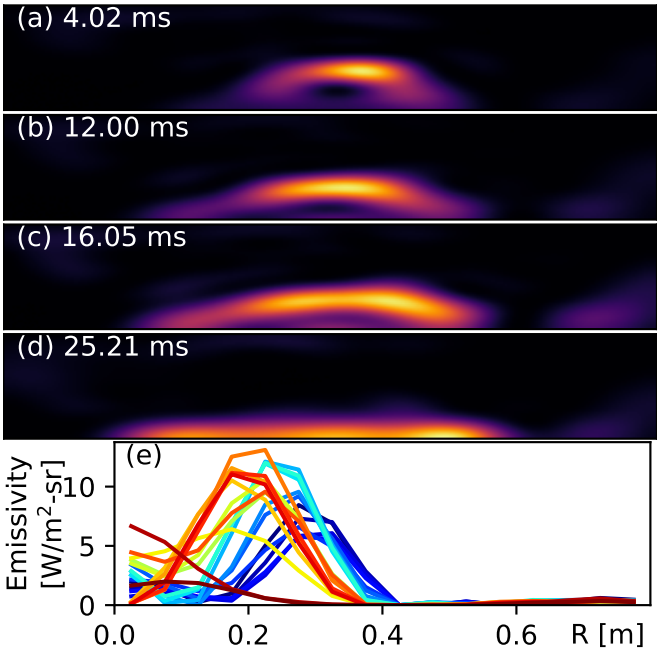

FIG. 3. (a)–(d) Reconstructed emissivity at several time points using both camera views of the confinement vessel. (e) Radial emissivity profiles at $z = 0$ for every millisecond from 3–25 ms.

The reconstruction is regularized using a correlated prior which imposes an anisotropic smoothness constraint and penalizes the magnitude of the reconstructed emissivity at large radii. A noise model is used to weight each pixel in the reconstruction. This model incorporates a constant and a term proportional to the pixel radiance which are added in quadrature to the camera discretization uncertainty and shot noise. Finally, the reconstructed emissivity values are obtained by nonnegative least squares fitting to minimize the residual.

Fig. 3a–d shows the reconstructed emissivity at several time points of a sample shot. The quality of the reconstruction can be examined by comparing the measured radiance (Fig. 4a and d) with the radiance determined by back-projecting the emissivity (Fig. 4b and e). Residuals are typically withing ±15%.

IV. DIVERTOR PLASMA VISUALIZATION

Concentric electrodes in the divertor vessels are electrically biased (up to -3.5 kV) in order to generate a radial electric field. The resulting radial current induces a torque on the open field-line plasma causing it to spin-up until an equilibrium is reached where the applied torque is balanced by drag (primarily from neutral ionization and charge-exchange). Magnetic field lines near the axis are typically biased negatively (inward pointing E_r) so that rotation is opposite the ion diamagnetic direction. This has been shown to stabilize azimuthal $n = 2$ deformations of the FRC which are deleterious to fast ion

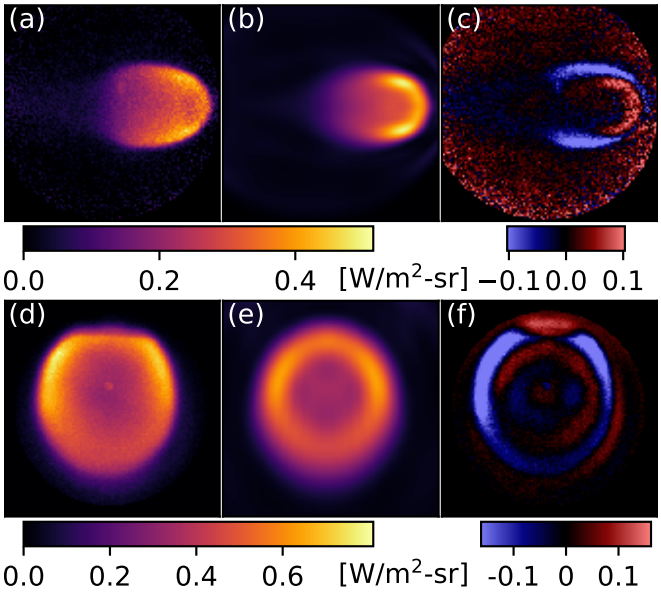

FIG. 4. Measured radiance, radiance projected from emissivity, and residual from (a-c) radial camera and (d-f) axial camera.

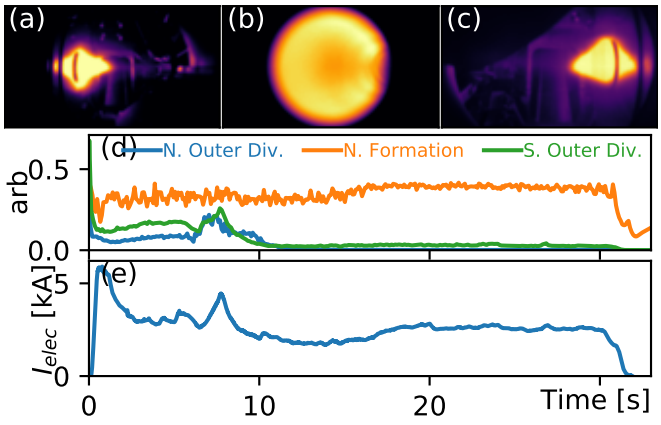

FIG. 5. Balmer-α images of the (a) north outer divertor, (b) north formation section, and (c) south outer divertor. (d) Total ionization rate in each region. (e) Electrode power supply current.

confinement. In addition, a GDT-style plasma gun is mounted behind a central orifice in the electrodes which can provide an initial plasma and/or gas source for biasing.

The divertors are equipped with cameras in order to visualize both the divertor plasma and discharges on the electrode surfaces. Ionization in front of the plasma gun orifice (Fig. 5a,c) is constrained within a conical profile due to the magnetic field expansion in the divertors. There is also significant ionization in the formation sections (Fig. 5b) since most fueling is injected in this region. The total ionization rate in each section is in Fig. 5(d) and the electrode bias power supply current (voltage was approximately held fixed at 2.1 ± 0.2 kV). Power supply current is clearly correlated with total ionization, but other factors such as the initial particle load from the theta-pinch formation process also play a role.

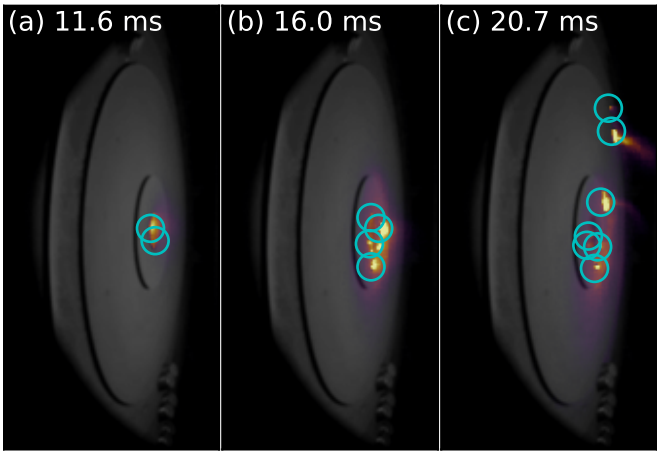

FIG. 6. Images of the 553.3 nm spectral line from Mo^{0+} 5p→5s overlaid on a grayscale image of the electrodes. Circles are drawn around the location of arcs determined from automated image processing.

Unfortunately, the combination of gas and/or plasma accumulation in the electrode gaps, heating from ion bombardment, and high voltage differences between neighboring electrodes occasionally leads to arcing. Not all arcs lead to power supply overcurrent, so potential arcs are identified by image processing. Besides narrowband filters for Balmer line emission, the cameras contain filters for O 1+, Ti 0+ (corresponding to getter material), and Mo 0+ (used in the plasma gun). After thresholding, local maxima are found and categorized based on the intensity of light emission and their location. Fig. 6 shows sample images and automated analysis results for a peculiar shot where arcing first occured in the plasma gun orifice, then propagated to the boundary of the inner electrode, then migrated to the boundary of the subsequent electrode. By automatically catching these off-normal events, the operations staff can be notified to take action to minimize possible damage to the machine on the subsequent shot.

We thank our shareholders for their support and trust, Google research, and all fellow TAE staff for their dedication, excellent work, and extra efforts.

[1]H. Gota, M. Binderbauer, T. Tajima, S. Putvinski, M. Tuszewski, B. Deng, S. Dettrick, D. Gupta, S. Korepanov, R. Magee, T. Roche, J. Romero, A. Smirnov, V. Sokolov, Y. Song, L. Steinhauer, M. Thompson, E. Trask, A. V. Drie, X. Yang, P. Yushmanov, K. Zhai, I. Allfrey, R. Andow, E. Barraza, M. Beall, N. Bolte, E. Bomgardner, F. Ceccherini, A. Chirumamilla, R. Clary, T. DeHaas, J. Douglass, A. DuBois, A. Dunaevsky, D. Fallah, P. Feng, C. Finucane, D. Fulton, L. Galeotti, K. Galvin, E. Granstedt, M. Griswold, U. Guerrero, S. Gupta, K. Hubbard, I. Isakov, J. Kinley, A. Korepanov, S. Krause, C. Lau, H. Leinweber, J. Leuenberger, D. Lieurance, M. Madrid, D. Madura, T. Matsumoto, V. Matvienko, M. Meekins, R. Mendoza, R. Michel, Y. Mok, M. Morehouse, M. Nations, A. Necas, M. Onofri, D. Osin, A. Ottaviano, E. Parke, T. Schindler, J. Schroeder, L. Sevier, D. Sheftman, A. Sibley, M. Signorelli, R. Smith, M. Slepchenkov, G. Snitchler, J. Titus, J. Ufnal, T. Valentine, W. Waggoner, J. Walters, C. Weixel, M. Wollenberg, S. Ziaei, L. Schmitz, Z. Lin, A. Ivanov, T. Asai, E. Baltz, and J. Platt, Nuclear Fusion **59**, 112009 (2019).

[2]P. G. Carolan, A. Patel, N. J. Conway, R. J. Akers, C. A. Bunting, G. F. Counsell, J. Dowling, M. R. Dunstan, A. Kirk, F. Lott, M. N. Price, M. R. Tournianski, and M. J. Walsh, Review of Scientific Instruments **75**, 4069 (2004).

[3]F. Scotti, *Modifications of impurity transport and divertor sources by lithium wall conditioning in the National Spherical Torus Experiment*, Ph.D. thesis, Princeton University, Princeton, NJ (2014).

[4]J. Harhausen, A. Kallenbach, C. Fuchs, and the ASDEX Upgrade Team, Plasma Physics and Controlled Fusion **53**, 025002 (2011).

[5].

[6]M. Binderbauer, T. Tajima, L. Steinhauer, E. Garate, M. Tuszewski, L. Schmitz, H. Guo, A. Smirnov, H. Gota, D. Barnes, B. Deng, M. Thompson, E. Trask, X. Yang, S. Putvinski, N. Rostoker, R. Andow, S. Aefsky, N. Bolte, D. Bui, F. Ceccherini, R. Clary, A. Cheung, K. Conroy, S. Dettrick, J. Douglass, P. Feng, L. Galeotti, F. Giammanco, E. Granstedt, D. Gupta, S. Gupta, A. Ivanov, . J. Kinley, K. Knapp, S. Korepanov, M. Hollins, R. Magee, R. Mendoza, Y. Mok, A. Necas, S. Primavera, M. Onofri, D. Osin, N. Rath, T. Roche, J. Romero, J. Schroeder, L. Sevier, A. Sibley, Y. Song, A. V. Drie, J. Walters, W. Waggoner, P. Yushmanov, K. Zhai, and the TAE Team, Physics of Plasmas **22**, 056110 (2015).

[7]H. Gota, M. W. Binderbauer, T. Tajima, S. Putvinski, M. Tuszewski, S. Dettrick, E. Garate, S. Korepanov, A. Smirnov, M. C. Thompson, E. Trask, X. Yang, L. Schmitz, Z. Lin, A. A. Ivanov, T. Asai, I. Allfrey, R. Andow, M. Beall, N. Bolte, D. Q. Bui, M. Cappello, F. Ceccherini, R. Clary, A. H. Cheung, K. Conroy, B. H. Deng, J. Douglass, A. Dunaevsky, P. Feng, D. Fulton, L. Galeotti, E. Granstedt, M. Griswold, D. Gupta, S. Gupta, K. Hubbard, I. Isakov, J. S. Kinley, K. Knapp, R. Magee, V. Matvienko, R. Mendoza, Y. Mok, A. Necas, S. Primavera, M. Onofri, D. Osin, N. Rath, T. Roche, J. Romero, T. Schindler, J. H. Schroeder, L. Sevier, D. Sheftman, A. Sibley, Y. Song, L. C. Steinhauer, T. Valentine, A. D. V. Drie, J. K. Walters, W. Waggoner, P. Yushmanov, K. Zhai, and T. T. Team, Nuclear Fusion **57**, 116021 (2017).

[8]M. Tuszewski, A. Smirnov, M. C. Thompson, S. Korepanov, T. Akhmetov, A. Ivanov, R. Voskoboynikov, L. Schmitz, D. Barnes, M. W. Binderbauer, R. Brown, D. Q. Bui, R. Clary, K. D. Conroy, B. H. Deng, S. A. Dettrick, J. D. Douglass, E. Garate, F. J. Glass, H. Gota, H. Y. Guo, D. Gupta, S. Gupta, J. S. Kinley, K. Knapp, A. Longman, M. Hollins, X. L. Li, Y. Luo, R. Mendoza, Y. Mok, A. Necas, S. Primavera, E. Ruskov, J. H. Schroeder, L. Sevier, A. Sibley, Y. Song, X. Sun, E. Trask, A. D. Van Drie, J. K. Walters, M. D. Wyman, and The TAE Team, Physical Review Letters **108**, 255008 (2012).

[9]M. Tuszewski, A. Smirnov, M. C. Thompson, T. Akhmetov, A. Ivanov, R. Voskoboynikov, D. Barnes, M. W. Binderbauer, R. Brown, D. Q. Bui, R. Clary, K. D. Conroy, B. H. Deng, S. A. Dettrick, J. D. Douglass, E. Garate, F. J. Glass, H. Gota, H. Y. Guo, D. Gupta, S. Gupta, J. S. Kinley, K. Knapp, S. Korepanov, A. Longman, M. Hollins, X. L. Li, Y. Luo, R. Mendoza, Y. Mok, A. Necas, S. Primavera, E. Ruskov, L. Schmitz, J. H. Schroeder, L. Sevier, A. Sibley, Y. Song, X. Sun, E. Trask, A. D. Van Drie, J. K. Walters, and M. D. Wyman, Physics of Plasmas **19**, 056108 (2012).

[10]E. M. Granstedt, P. Petrov, K. Knapp, M. Cordero, and V. Patel, Review of Scientific Instruments **87**, 11D416 (2016).

[11]E. M. Granstedt, D. Fallah, and M. C. Thompson, Review of Scientific Instruments **89**, 10E103 (2018).